Journal of Power Sources 523 (2022) 231030

Contents lists available at ScienceDirect

Journal of Power Sources

journal homepage: www.elsevier.com/locate/jpowsour

Porous nitrogen-doped graphene nanofibers comprising metal organic framework-derived hollow and ultrafine layered double metal oxide nanocrystals as high-performance anodes for lithium-ion batteries

Chan Sic Kim [a,1], Jae Seob Lee [a,1], Rakesh Saroha [a], Yoon Beom Park [a], Yun Chan Kang [b], Dong-Won Kang [c], Sang Mun Jeong [d,**], Jung Sang Cho [a,*]

[a] Department of Engineering Chemistry, Chungbuk National University, 1, Chungdae-Ro, Seowon-Gu, Cheongju-Si, Chungbuk, 361-763, Republic of Korea
[b] Department of Materials Science and Engineering, Korea University, 145, Anam-Ro, Seongbuk-Gu, Seoul, 02841, Republic of Korea
[c] School of Energy Systems Engineering, Chung-Ang University, 84, Heukseok-Ro, Dongjak-Gu, Seoul, 06974, Republic of Korea
[d] Department of Chemical Engineering, Chungbuk National University, 1, Chungdae-Ro, Seowon-Gu, Cheongju-Si, Chungbuk, 361-763, Republic of Korea

HIGHLIGHTS

- Hierarchically porous and multicomponent structure as anodes for Li ion batteries.
- Nanostructure comprises N-doped graphene and hollow layered double oxide crystals.
- Detailed formation mechanism of the nanofibers is investigated.
- Unique architecture shows excellent Li ion storage properties.

GRAPHICAL ABSTRACT

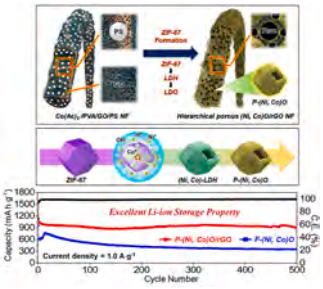

ARTICLE INFO

Keywords:
Lithium ion batteries
Anode materials
Electrospinning
Metal-organic framework
Layered double metal oxide

ABSTRACT

The growth of unique nanostructures with multicomponent systems is a renowned strategy for developing advanced materials for various energy storage applications. Herein, we utilize a facile approach to synthesize multicomponent high-performance nanofibers as anodes that comprises hierarchically porous and self-supporting N-doped reduced graphene oxide (N-doped rGO) matrix grafted with metal-organic framework (MOF)-derived hollow and ultrafine layered double metal (Ni and Co) oxide (LDO) nanocrystals [P-(Ni, Co)O/rGO NFs]. The porous and highly conductive N-doped rGO scaffold not only provides structural integrity but also offers short Li-ion diffusion pathways along with enormous conductive channels for rapid charge transfer during cycling. The hollow and ultrafine LDO nanocrystals also provide sufficient space for rapid reaction sites and to absorb the severe volume stress generated during repeated charge-discharge cycles owing to their rich oxidation states. The Li-cell utilizing the P-(Ni, Co)O/rGO NFs as anodes exhibits overall enhanced electrochemical performance with prolonged cycling stability (907 mA h g^{-1} at the end of 500th cycle) and a satisfactory high-rate capability (519 mA h g^{-1} at 5.0 A g^{-1}).

* Corresponding author.
** Corresponding author.
E-mail addresses: smjeong@chungbuk.ac.kr (S.M. Jeong), jscho@chungbuk.ac.kr (J.S. Cho).
[1] These authors contributed equally to this work.

https://doi.org/10.1016/j.jpowsour.2022.231030
Received 6 November 2021; Received in revised form 4 January 2022; Accepted 13 January 2022
Available online 24 January 2022

1. Introduction

The development of advanced rechargeable energy storage systems is always a priority for matching the ever-increasing demand for energy [1–4]. Recently, layered double hydroxide (LDH) nanostructures have aroused considerable interests for a wide range of applications in electrocatalysis, drug delivery, and supercapacitor due to their unique structure characteristics [5]. The LDH nanostructures are considered as two-dimensional (2D)-layered materials that are similar to hydrotalcite-like structures and formed due to the intercalation of one metal hydroxide layer within the second metal hydroxide. Such double layered arrangement normally allows large accessible surface areas, tunable morphology, and high charge density [5–7]. However, with regard to lithium ion batteries (LIBs) anode materials, its poor electronic conductivity ($<10^{-3}$ S cm^{-1}) and the severe aggregation of LDH layers prohibit rapid Li-ion transfer, and therefore, slow redox processes [7].

To overcome these drawbacks, numerous efficient strategies have been adopted which includes rational nanostructures with different morphologies [8,9], different synthesis techniques [6,9], carbon material coating, and carbon composites [10,11]. However, among all the synthesis techniques, the metal-organic framework (MOF)-derived LDH technique has been widely used owing to its simplistic approach [12]. MOFs are a class of three-dimensional (3D) porous materials comprising a central core metal ion surrounded by organic molecules [13–17]. In particular, MOFs act as sacrificial templates and sources of metal precursors for the formation of 3D hollow LDH frameworks comprising ultrafine nanocrystals [12]. As an anode material, the MOF-derived LDH framework possesses a large specific surface area, which not only provides enough space to absorb severe volume variations but also alleviates particle agglomeration besides offering efficient electrolyte penetration and short diffusion pathways during the charge-discharge process [18]. Furthermore, the low electronic conductivity can be increased by concomitant conversion of LDHs to layered double metal oxides (LDO) using a simple low-temperature heat-treatment process in air. During the oxidation process, LDHs compounds decomposes into a mixture of oxides, in which one layered oxide is intercalated with another layered oxide, generating a pattern that is similar to the LDH pattern. Moreover, one-order higher electronic conductivity of the LDO phases (10^{-3}–10^{-2} S cm^{-1}) compared to the LDH phase improves the reaction kinetics and allows comparatively faster Li-ion diffusion [19,20]. Additionally, the LDO nanostructure composed of binary transition metal oxides such as Ni–Co oxides, believed to have high redox activities owing to their rich oxidation states [21–24].

Herein, we utilized a combined strategy of synthesizing multicomponent nanostructures containing hierarchically porous N-doped reduced graphene oxide (N-doped rGO) matrixed nanofibers, which comprise hollow and ultrafine layered double metal (Ni and Co) oxide nanocrystals [denoted as P-(Ni, Co)O/rGO NFs] derived from the MOF-based hollow LDH nanostructure. The unique nanostructure introduced in this study was analyzed for its potential as a high-performance anode material for LIBs. The stabilized (Ni, Co)-LDH nanostructure acted as a precursor for the metal source, whereas a polystyrene (PS) nanobead suspension ($\varphi = 40$ nm) was used as a mesopore-forming agent. Likewise, graphene oxide (GO) nanosheets were used to form a self-supporting matrix to enhance the integrity and electrical conductivity of the nanofibers as anode materials during cycling. During the heat treatment, the PS nanobeads were decomposed thus leaving pores behind whereas the GO nanosheets were transformed into an N-doped rGO skeleton comprising hollow ultrafine LDO nanocrystals obtained from the stabilized LDH nanostructure. The hierarchical porous nanostructure together with the hollow nanocrystals provides enough space to channel off the volume variation stress during the redox processes and also allows better electrolyte percolation to eventually enhance Li-ion diffusion due to shorter diffusion pathways which subsequently resulted in stable cycling performance [25,26]. Likewise, the N-doped rGO matrix ensures high electrical conductivity and rapid charge transfer, thereby favoring fast electrochemical reactions.

Benefitting from the unique nanostructure design, the P-(Ni, Co)O/rGO NFs displayed a superior electrochemical performance with higher rate capabilities and long-term cycling stability compared to the composite nanofibers prepared without PS nanobeads, GO nanosheets, and stabilized LDH nanostructures, that is, the filled-type (non-porous) and biphasic structure [denoted as F-(Ni, Co)O)]. To the best of our knowledge, such a rational nanostructure design strategy for obtaining hollow layered double metal oxide nanocrystals encapsulated in a highly conductive N-doped rGO framework as an advanced LIB anode has not been reported to date. Therefore, we believe that the structural and electrochemical results presented in this work will provide insight into the fabrication of multicomponent and highly sustainable advanced materials for various rechargeable energy storage systems.

2. Experimental section

Sample Preparation: Hierarchically porous N-doped rGO nanofibers comprising hollow LDO nanocrystals were prepared using an electrospinning technique followed by post-treatment. For electrospinning solution, 0.5 g of GO nanosheets were ultrasonicated in 30 mL of ethanol for 6 h to form a homogeneous suspension. Afterward, a 20 mL PS nanobeads suspension solution, 6.0 g of cobalt acetate tetrahydrate ($Co(Ac)_2.4H_2O$, Daejung, 98.0%, Mw = 291.02), and 3.0 g of polyvinyl alcohol (PVA 2000, Kanto Chemical Co.) were sequentially added to the suspension. The suspension was stirred for 24 h to obtain a uniform dispersion. The size-controlled PS nanobeads ($\varphi = 40$ nm) were prepared using an emulsion-free polymerization technique [27]. GO nanosheets were also obtained from graphite flakes using a modified Hummer's method that was reported previously [28]. The spinning solution was then loaded into a plastic syringe pump (12 mL capacity) fitted with a 21-gauge stainless steel needle. The spinning solution was ejected at a speed of 4.0 mL h^{-1} and the fibers were collected onto a rotating drum (180 rpm) covered with Al foil, which was set at a distance of 15 cm from the tip of the needle. The voltage applied between the collector and the needle was fixed at 20 kV. The as-spun $Co(Ac)_2$/PVA/GO/PS composite nanofibers were stabilized at 100 °C for 30 min in a hot air oven. To grow ZIF-67 polyhedra over the nanofiber surface, 0.5 g of stabilized $Co(Ac)_2$/PVA/GO/PS nanofibers were added into 50 mL of a methanol solution mixed with 3.0 g of 2-methylimidazole (Wako Pure Chemical Industries Ltd., 98%) and were kept undisturbed for 24 h at ambient temperature. Afterward, the sample was washed repeatedly with ethanol and stabilized at 150 °C for 3 d in an air atmosphere to form ZIF-67/PVA/GO/PS composite nanofibers. A total of 0.1 g of stabilized ZIF-67/PVA/GO/PS composite nanofibers were treated with a stoichiometric amount (0.2 g) of nickel nitrate hexahydrate ($Ni(NO_3)_2{\cdot}6H_2O$, Daejung, 98.0%, Mw = 290.79) dissolved in ethanol (7 mL) and ultrasonicated for 1 h, followed by drying at 100 °C for 1 h in an air environment. This process resulted in the formation of a hollow (Ni, Co)-LDH nanostructure. The ZIF-67 derived hollow (Ni, Co)-LDH nanostructures were then heat-treated at 250 °C for 3 h in an air atmosphere to obtain hollow layered double oxide [(Ni, Co)-LDO] nanocrystals. The final product obtained was denoted as P-(Ni, Co)O/rGO NFs. A comparison sample was also prepared without PS nanobeads, GO nanosheets, and LDH nanostructures using an electrospinning technique with a spinning solution comprising stoichiometric amounts of nickel (2.4 g) salt, cobalt (3.6 g) salt, and PVA (3.0 g) in ethanol (30 mL) as the solvent. The stabilized Co/Ni/PVA composite nanofibers were subjected to single-step heat-treatment at 600 °C for 3 h in an air environment, which results in the formation of a bi-phasic mixed metal (Ni and Co) oxide nanostructure. This structure was abbreviated as F-(Ni, Co)O NFs, where "F" stands for filled-type morphology.

Characterization Techniques: The microstructural features of the as-prepared nanofibers were studied using field-emission scanning electron microscopy (FE-SEM, Ultra Plus, Zeiss) and field-emission transmission electron microscopy (FE-TEM, JEM-2100F, JEOL, KBSI). The phase

analysis of the nanofibers was performed using X-ray diffractometer (XRD, Bruker, D8 Discover) equipped with Cu $K_{\alpha 1}$ radiation (1.5405 Å) at the Korea Basic Science Institute (Daegu). The thermal stability was studied using thermogravimetric analysis (TGA, Pyris 1, PerkinElmer) in the temperature range of room temperature to 600 °C at a heating rate of 10 °C min^{-1} in an air atmosphere unless mentioned otherwise. The surface chemistry and bonding environment analysis of all the elements in the prepared nanofibers were carried out using an X-ray photoelectron spectroscopy (XPS, K-Alpha, Thermo Scientific) instrument with Al Kα radiation. The Brunauer–Emmett–Teller (BET) technique was employed to determine the surface area and pore volume of the nanofibers using N_2 adsorption-desorption isotherms. The structural properties and crystallinity of the carbonaceous material in the nanofibers were measured using Raman spectroscopy (LabRam, HR800, Horiba Jobin-Yvon).

Electrochemical Measurements: The prepared composite nanofibers were employed as anodes inside CR2032-type coin cells for electrochemical analysis. Briefly, a homogeneous slurry was prepared by mixing the composite nanofibers as active material, carbon black (Super-P) as a conductive agent, and sodium carboxymethyl cellulose as a binder in a 7:2:1 ratio in an appropriate amount of deionized water. The slurry was then cast on a copper current collector sheet using the doctor blade technique and dried at 60 °C overnight in a hot air oven to remove the solvent. Subsequently, circular discs (φ = 14 mm) were punched and used inside the coin cell as advanced anodes, with Li metal as the counter electrode and a microporous polypropylene film as the separator. The electrolyte used was 1.0 M $LiPF_6$ in a 1:1 v/v mixture of fluoroethylene carbonate and dimethyl carbonate (FEC/DMC). The cell

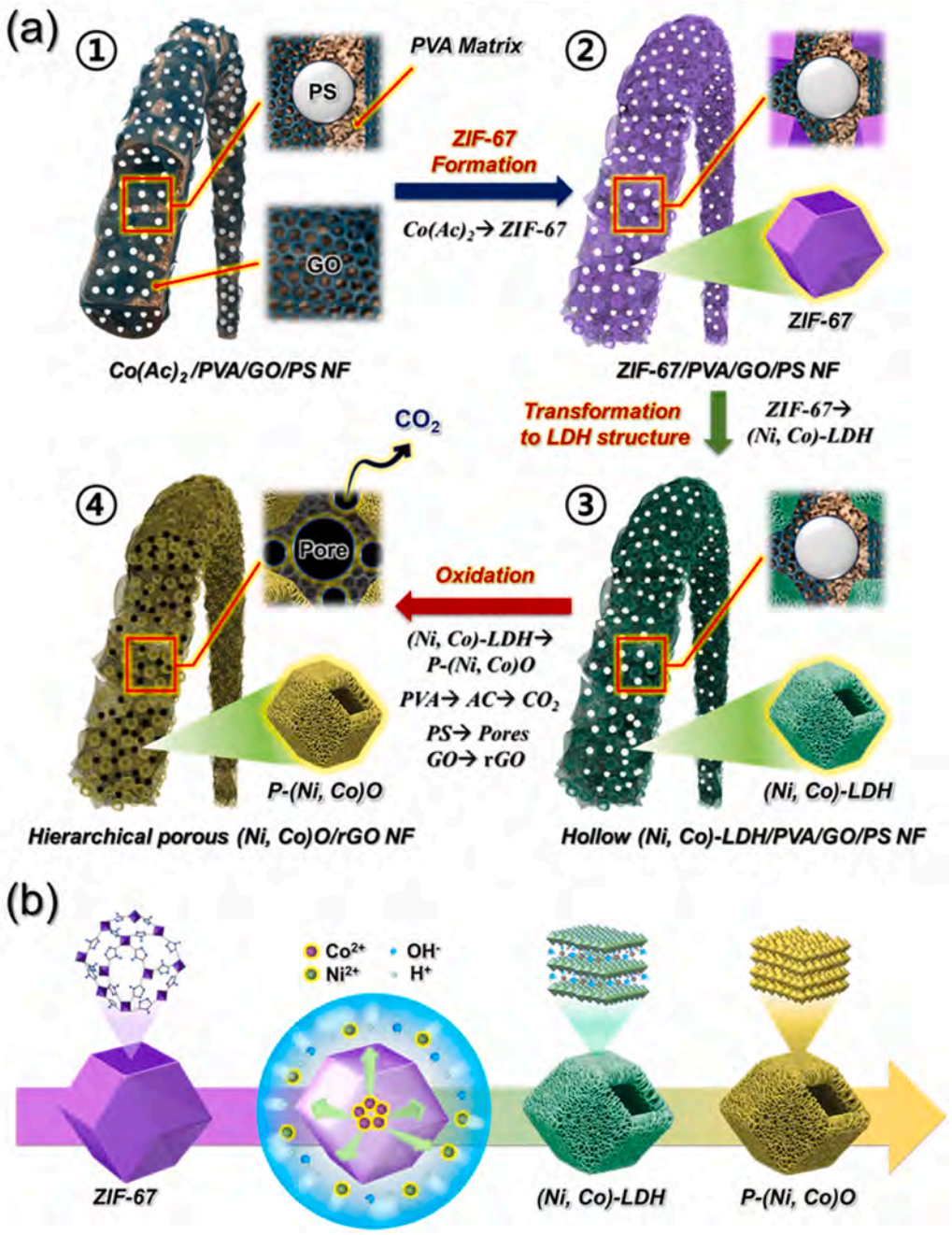

Scheme 1. (a) Schematic representation of the formation mechanism of the hierarchical porous N-doped rGO nanofibers comprising hollow and ultrafine layered double metal oxide nanocrystals and (b) detailed formation mechanism of the hollow layered double metal oxide nanocrystal as a precursor.

assembly was performed inside a glove box filled with high-purity argon gas. Cyclic voltammograms (CVs) were obtained at a scan rate of 0.1 mV s^{-1} using a WBCS3000 battery cycler (WonATech). The active material loading in the working electrode was fixed at *ca.* 0.5 mg cm^{-2} throughout the electrochemical tests. The galvanostatic discharge-charge characteristics of the nanofibers were acquired at different current densities from 0.5 to 5.0 A g^{-1} in the voltage window of 0.001–3.0 V. An electrochemical impedance spectrum (EIS) was obtained using an impedance analyzer in the frequency range of 100 kHz to 10 mHz with a pulse amplitude of 10 mV.

3. Results and discussion

Hierarchical porous N-doped rGO nanofibers comprising MOF-derived hollow and ultrafine LDO nanocrystals were synthesized using the electrospinning technique and subsequent post-treatment. The synthesis mechanism of the rational nanostructure is presented in Scheme 1a. First, the as-spun nanofibers comprising a uniform dispersion of Co $(Ac)_2$, GO nanosheets, and PS nanobeads in the PVA matrix were obtained using the conventional electrospinning technique (Scheme 1a-①). Thereafter, the stabilized $Co(Ac)_2$/PVA/GO/PS composite nanofibers were treated with 2-methylimidazole in methanol, which resulted in the uniform growth of the ZIF-67 nanocrystal all over the nanofiber surface owing to the strong interaction between the positively charged Co ions and the negatively charged 2-methylimidazole ligands (Scheme 1a-②). This interaction resulted in the formation of ZIF-67/PVA/GO/PS composite nanofibers with all the cobalt species were consumed during the growth of the ZIF-67 nanocrystals. Subsequently, the ZIF-67/PVA/GO/PS nanofibers were treated with nickel nitrate in ethanol, which resulted in strong coordination between ZIF-67 and Ni ions. The coordination between the different ionic species resulted in the formation of a hollow (Ni, Co)-LDH nanocrystal through chemical reactions induced by the self-sacrificing nature of the ZIF-67 template (Scheme 1a-③). A schematic representation of the detailed formation mechanism of the hollow (Ni, Co)-LDH and subsequent (Ni, Co)-LDO nanocrystal is presented in Scheme 1b. The $Ni(NO_3)_2{\cdot}6H_2O$ in ethanol solvent disintegrates into Ni^{2+} and NO_3^- ions in the presence of the ZIF-67/PVA/GO/PS composite nanofibers. The hydrolysis of Ni^{2+} ions in ethanol generates protons (H^+) that bonded with NO_3^- ions to form a slightly acidic medium. In addition, the NO_3^- ions also react with the ZIF-67 polyhedron that results in the oxidation of Co ions (from Co^{2+} to Co^{3+}) [29]. This persistent consumption of H^+ ions leads to an increased number density of $–OH^-$ species leading to a higher concentration of divalent and trivalent ions around the ZIF-67 surface. The coprecipitation of the metal ion species leads to the formation of an LDH layer with one metal hydroxide layer intercalated within another metal hydroxide layer. As the reaction proceeded, the inner core of the ZIF-67 nanocrystals was consumed during the process and resulted in the formation of a hollow nanocrystal surrounded by a layer of (Ni, Co)-LDH. Therefore, hollow (Ni, Co)-LDH/PVA/GO/PS nanofibers were obtained via MOF-sacrificing chemical reactions (Schemes 1a-③ and 1b). During the heat treatment of (Ni, Co)-LDH/PVA/GO/PS nanofibers in an air atmosphere, the hollow layered double hydroxide nanostructure was converted to ultrafine layered double metal (Ni, Co) oxide nanocrystals well-embedded in the composite (Schemes 1a-④ and 1b). In addition, the N-rich ligand groups of the (Ni, Co)-LDH nanocrystal act as a precursor for the N-doping source after the removal of organic linkers [30]. Therefore, the GO nanosheets in the composites were converted into N-doped rGO. Additionally, the PVA polymer was carbonized into amorphous carbon (AC) and finally burned off selectively, leaving mesopores. Likewise, the uniformly dispersed size-controlled PS nanobeads ($\varphi = 40$ nm) decomposed completely into gaseous products, thus forming numerous mesopores. Finally, hierarchical porous N-doped rGO nanofibers comprising hollow and ultrafine LDO nanocrystals, denoted as P-(Ni, Co)/rGO, were successfully obtained (Scheme 1a-④).

To understand the formation mechanism of the unique structured nanofibers, we carried out a systematic investigation of the microstructural and phase variations after each step. The morphological and phase analyses of the as-spun $Co(Ac)_2$/PVA/GO/PS composite nanofibers after stabilization at 150 °C are shown in Fig. S1. The composite nanofibers exhibited a continuous 1D fibrous morphology (Fig. S1a) with an average diameter of *ca.* 1.0 μm. In addition, a smooth nanofiber surface along with a filled cross-sectional image is also evident in Fig. S1b, which clearly suggests a homogeneous distribution of the metal salt, GO nanosheets, and PS nanobeads in the nanofiber structure. Notably, an efficient interaction among the acid-functionalized GO nanosheets, PVA, and PS nanobeads also resulted in highly integrated nanofibers. The XRD patterns of the composite nanofibers shown in Fig. S1c reveals a broad peak around $2\theta = 24°$, highlighting the amorphous nature of the composite nanofibers. The presence of the GO nanosheets inside the fiber structure was further confirmed by Raman spectra, as shown in Fig. S1d, which clearly have broad peaks that are typical signatures of the D-band (1346 cm^{-1}) and G-band (1600 cm^{-1}) of the GO phase [30]. Moreover, a relative intensity ratio (i.e., I_D/I_G) value of 0.99 is also indicative of the amorphous nature of the carbon.

The as-spun $Co(Ac)_2$/PVA/GO/PS composite nanofibers were employed as a self-supporting matrix for the efficient formation of ZIF-67 nanocrystals on the surface of the nanofibers. The $Co(Ac)_2$/PVA/GO/PS composite nanofibers were reacted with a 2-methylimidazole solution and dried to remove the solvent. The resulting ZIF-67/PVA/GO/PS nanofibers were analyzed using various physical characterizations to elucidate the changes they underwent, as shown in Fig. 1. The composite nanofiber 1D morphology (Fig. 1a and b) remained intact with an increase in mean diameter (*ca.* 2.0 μm) owing to the growth of numerous nanocrystals on the fiber surface. Besides, the presence of the GO sheets was also evident, as shown in the cross-sectional FE-SEM image of ZIF-67/PVA/GO/PS nanofiber (Fig. S2). ZIF-67 nanocrystals ($\varphi = 70$ nm) (Fig. 1c) grew homogeneously throughout the nanofiber surface, as shown in Fig. 1c and d. This could be attributed to the strong interaction between the negatively charged 2-methyimidazole units as organic linkers and the positively charged metallic Co ions as central atoms, which were present in the $Co(Ac)_2$/PVA/GO/PS composite nanofibers and collectively enabled the growth of ZIF-67 nanocrystals. The XRD pattern shown in Fig. 1f has sharp peaks associated with phase-pure ZIF-67 nanocrystals [31]. Furthermore, the elemental dot mapping results presented in Fig. 1g suggest uniform dispersion of Co, O, C, and N along the fiber length, indicating homogeneous deposition of the ZIF-67 nanocrystals over the fiber nanostructure.

The ZIF-67/PVA/GO/PS composite nanofibers with well-grown ZIF-67 nanocrystals over the fiber surface were further treated with an ethanol solution containing an appropriate amount of Ni salt, as described in Scheme 1a-③ and 1b to obtain hollow (Ni, Co)-LDH/PVA/GO/PS. The Ni-salt-treated composite nanofibers with the ZIF-67 deposited nanocrystals are shown in Fig. 2. The composite nanofibers maintained their 1D nanostructure (Fig. 2a and b) with a mean diameter of *ca.* 2.0 μm. However, uniform deposition of the well-grown layered-structured (Ni, Co)-LDH hollow nanocrystal ($\varphi = 100$ nm) over the nanofiber surface was observed, as shown in Fig. 2b and c. The TEM images shown in Fig. 2d–f clearly have dark and bright regions corresponding to the (Ni, Co)-LDH and hollow regions, respectively. The (Ni, Co)-LDH nanocrystals with clear lattice fringes separated by 0.25 nm for the (012) crystal plane are evident in the HR-TEM image shown in Fig. 2g. Furthermore, the selected area electron diffraction pattern (SAED) (Fig. 2h) and XRD pattern in Fig. 2i further indicate the formation of the (Ni, Co)-LDH phase only, which matches well with previously published studies [32–35]. The elemental-mapping images presented in Fig. 2j indicate the homogeneous dispersion of Ni in the nanofiber structure along with Co, O, C, and N, thus suggesting the uniform formation of the layered (Ni, Co)-LDH over the nanofiber surface. Additionally, the carbon content of the composite was quantified using TG analysis (Fig. S3a), and *ca.* 81 wt% primarily due to the PVA and GO nanosheets in the structure.

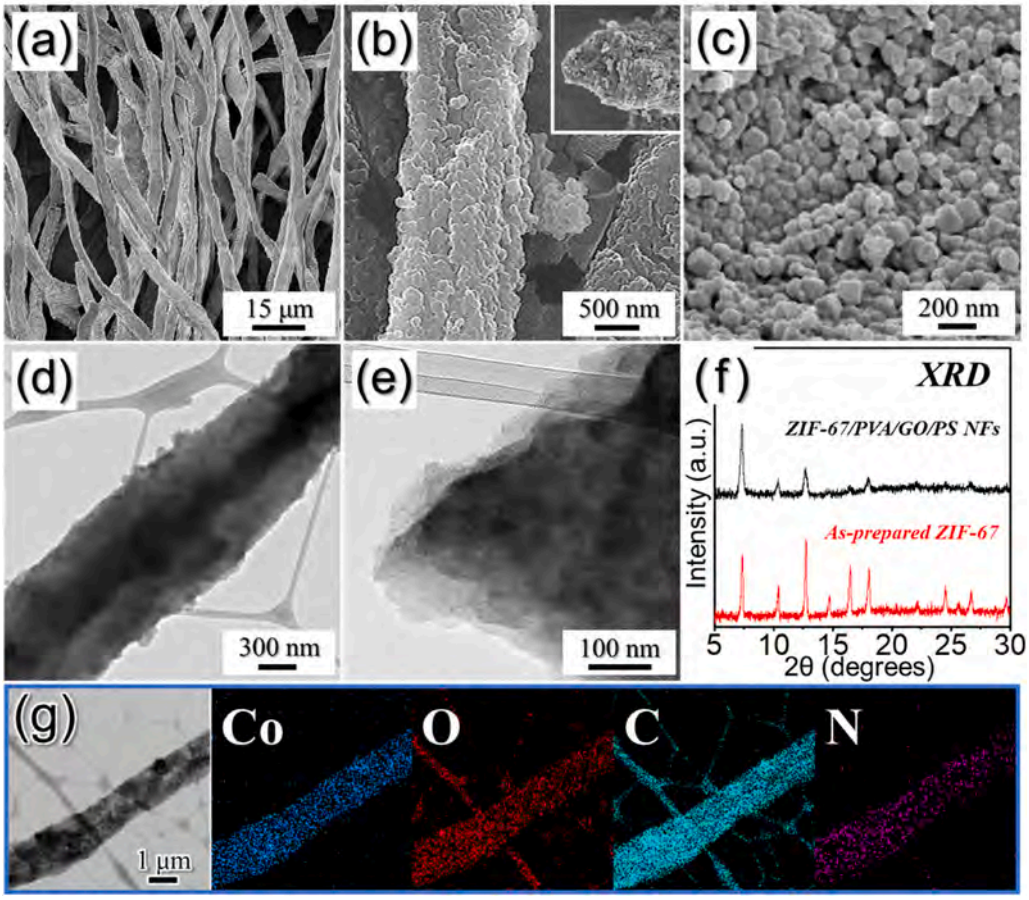

Fig. 1. Morphological and phase analysis of the ZIF-67/PVA/GO/PS composite nanofibers: (a, b) FE-SEM micrographs, (c) high-resolution FE-SEM image, (d, e) TEM images, (f) XRD pattern, and (g) elemental dot mapping images.

Hierarchically porous N-doped rGO nanofibers comprising hollow and ultrafine LDO nanocrystals [P-(Ni, Co)O/rGO NFs] were finally obtained after heat treatment of the hollow (Ni, Co)-LDH/PVA/GO/PS composite nanofibers at 250 °C, as shown in Fig. 3. During the oxidation process, the hollow (Ni, Co)-LDH nanocrystals were converted into a layered double metal oxide [(Ni, Co)-LDO] in air. Additionally, the PVA polymer was converted to amorphous carbon and subsequently burned off. The selective decomposition of PVA via CO_2 release form voids in the nanostructure. Likewise, the decomposition of the PS nanobeads resulted in a hierarchical porous structure with mesopores (10 nm) uniformly distributed in the structure. The rGO nanosheets act as a self-supportive matrix that guarantees the structural integrity of the nanofiber structure and allows rapid charge transfer during electrochemical processes owing to its high electrical conductivity. The FE-SEM micrographs shown in Fig. 3a and b indicate that the final nanostructure still maintains a 1D fibrous morphology even after oxidation, with the nanofiber surface covered with hollow (Ni, Co)-LDO nanocrystals, as shown in Fig. 3c. The TEM images shown in Fig. 3d–f again confirm the fibrous nanostructure with a diameter of 400 nm and deposited with ultrafine hollow (Ni, Co)-LDO nanocrystals (Fig. 3f). During oxidation at 250 °C, both the removal of PVA in the composite and the simultaneous sintering process resulted in shrinkage of the nanofibers from 2.0 μm to 400 nm. The HR-TEM image shown in Fig. 3g clearly indicates a lattice fringe separated by 0.21 nm for the lattice plane (200) corresponding to the hollow (Ni, Co)-LDO ultrafine nanocrystals. The SAED (Fig. 3h) and XRD (Fig. 3i) patterns further confirm the successful formation of the (Ni, Co)-LDO phase only, which is consistent with previous reports [36]. The elemental mapping images presented in Fig. 3j indicate homogeneous distribution of Ni, Co, O, C, and N along the fiber length, suggesting the formation of hollow (Ni, Co)-LDO ultrafine nanocrystals throughout the nanostructure. Overall, the systematic synthesis design resulted in nanofibers that primarily comprised hierarchically porous MOF-derived hollow (Ni, Co)-LDO ultrafine nanocrystals and a self-supportive N-doped rGO matrix as an advanced anode for LIBs.

The surface chemical environment of the various elements in the prepared P-(Ni, Co)O/rGO NFs was studied using XPS, as shown in Fig. 4. The XPS survey spectrum in Fig. 4a shows photoelectron signals corresponding to the Ni 2p, Co 2p, O 1s, N 1s, and C 1s chemical states. The Ni 2p XPS spectrum in Fig. 4b indicates the existence of well-resolved Ni $2p_{3/2}$ (853.9 eV) and Ni $2p_{1/2}$ (872.2 eV) peaks arising from spin-orbit splitting [37–39]. The deconvolution of Ni $2p_{3/2}$ and Ni $2p_{1/2}$ indicates further peak splitting, which suggests the presence of Ni^{2+} and Ni^{3+} oxidation states [40–42]. Moreover, the appearance of two shakeup satellite peaks (denoted as "Sat.") at 860.8 and 879.1 eV confirms the presence of NiO species [43–45]. Furthermore, similar results were observed for the Co 2p XPS signal (Fig. 4c), which had two well-separated photoelectron peaks for Co $2p_{3/2}$ (779.6 eV) and Co $2p_{1/2}$ (795.6 eV) flanked by the respective satellite signals at 785.4 and 802.2 eV, thus suggesting the formation of Co_3O_4 [30,46,47]. In addition, the existence of divalent and trivalent Co species is also evident from the splitting of Co $2p_{3/2}$ and Co $2p_{1/2}$ [48]. These results are consistent with the previously reported XPS profiles of the (Ni, Co)-LDO nanostructure [49]. The C 1s XPS profile in Fig. 4d has three well-fitted peaks at binding energies of 284.1, 285.1, and 288.0 eV that could be assigned to -C═C-, -C-N/C–C-, and -C═O-, respectively [30,46]. In addition, the deconvoluted -C-N/C–C- peak signifies N-doping in the nanostructure, which offers improved electrical conductivity due to the high electronegativity of the N atom [30]. This observation was further supported by

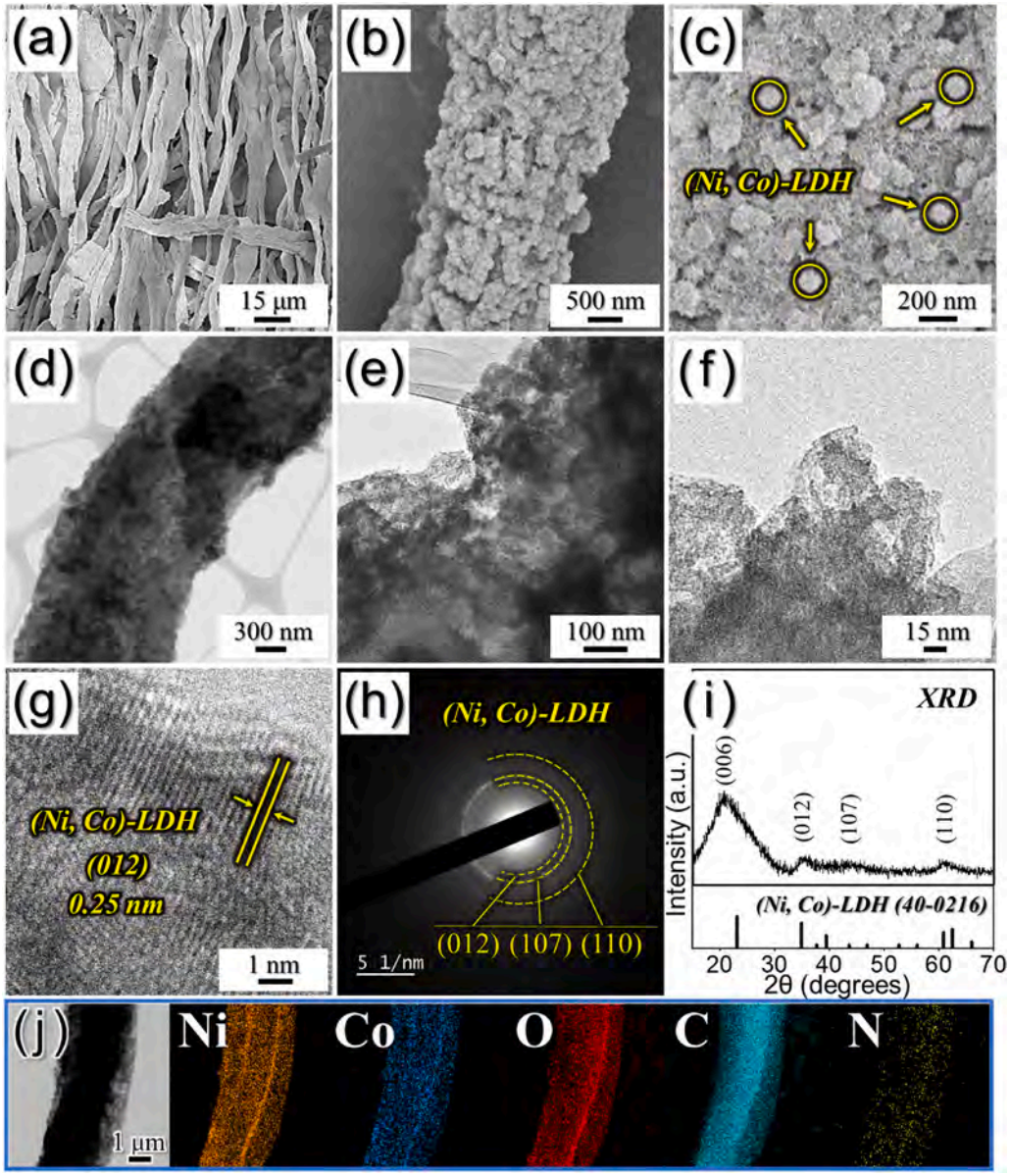

Fig. 2. Morphological and phase analysis of the (Ni, Co)-LDH/PVA/GO/PS composite nanofibers: (a, b) FE-SEM micrographs, (c) high-resolution FE-SEM image, (d–f) TEM images, (g) HR-TEM image, (h) SAED pattern, (i) XRD pattern, and (j) elemental dot mapping images.

the N 1s XPS spectrum (Fig. 4e), which indicates the existence of four peaks with different nitrogen environments, that is, pyridinic N (398.5 eV), pyrrolic N (399.7 eV), graphitic N (401.0 eV), and oxidized N (403.2 eV) [50]. In general, N doping enhances the electrical conductivity, which results in fast charge transfer during the redox processes. The quantity of N in the composite was 2.7 wt% from the elemental analysis (EA) results (Table S1). The crystallinity of the carbon products of the P-(Ni, Co)O/rGO NFs was also analyzed using Raman spectroscopy (Fig. 4f), which indicated a typical D-band (1353 cm^{-1}) and G-band (1600 cm^{-1}) [51]. The relative intensity ratio (I_D/I_G) determines the nature of the carbonaceous material in the sample. The I_D/I_G ratio of 0.87 indicates that the carbon products in the prepared nanofibers are mainly graphitic in nature, which induces high electrical conductivity. Furthermore, the C content in the nanofibers was determined by TG analysis, as shown in Fig. S3b, which was *ca.* 34 wt% and matches well with the EA results shown in Table S1. The BET surface area of the P-(Ni, Co)O/rGO NFs was 59 m^2 g^{-1}, as shown in Fig. S4a. In addition, the Barrett–Joyner–Halenda pore-size distributions (Fig. S4b) indicates the presence of a broad peak for mesoporous reason in the structure. The broad distribution of mesopores was formed primarily due to both the decomposition of the PS nanobeads and the uniform distribution of the PVA matrix during oxidation.

For better comparison, composite nanofibers without LDH nanocrystals were prepared using the electrospinning technique. The as-spun Co/Ni/PVA composite precursor nanofibers stabilized at 150 °C were subjected to oxidation at 600 °C, and the resulting nanofibers are shown in Fig. S5. The 1D fibrous morphology is evident in the FE-SEM micrographs shown in Figs. S5a and S5b, with an average diameter of 400 nm. The TEM image in Fig. S5c displays nanofibers with a filled morphology, which is consistent with the FE-SEM micrographs. The HR-TEM image in Fig. S5d indicates a lattice fringe that is sufficiently separated by 0.21 nm and 0.29 nm for the (012) and (220) crystal plane of the NiO and Co_3O_4 phases, respectively. The SEAD patterns shown in Fig. S5e clearly displays the diffraction planes corresponding to both the NiO and Co_3O_4 phases. Furthermore, the XRD pattern in Fig. S5f is in good agreement with the SAED pattern, exhibiting sharp peaks attributed to the NiO and Co_3O_4 crystal structures. The elemental dot mapping images (Fig. S5g) suggest the homogeneous dispersion of the Ni, Co, and O elements in the

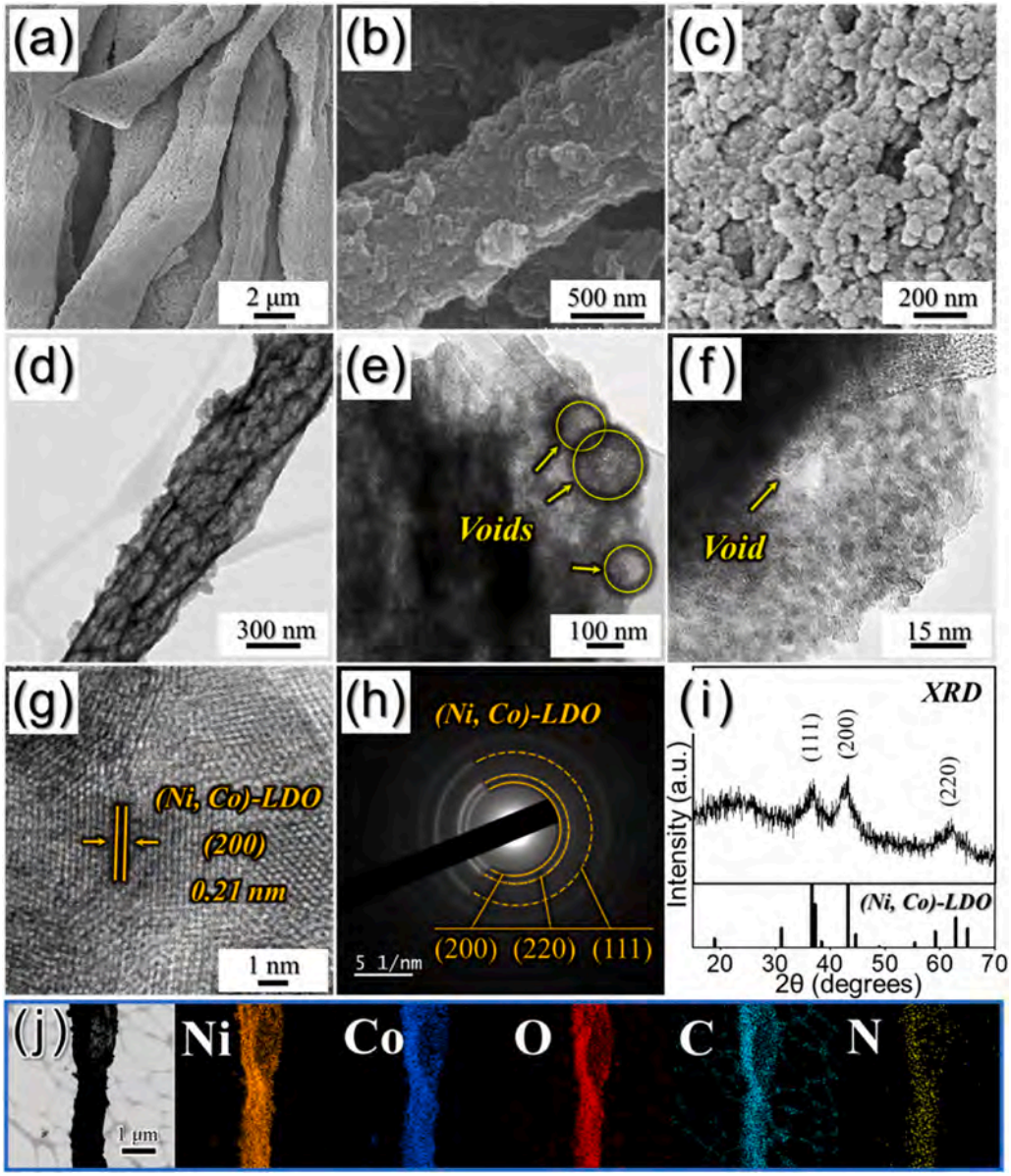

Fig. 3. Morphological and phase analysis of the P-(Ni, Co)O/rGO NFs: (a, b) FE-SEM micrographs, (c) high-resolution FE-SEM image, (d–f) TEM images, (g) HR-TEM image, (h) SAED pattern, (i) XRD pattern, and (j) elemental dot mapping images.

prepared nanofibers. Moreover, the carbon was completely removed from the structure at 600 °C. The C element visualized in the elemental mapping image is due to the presence of a carbon grid for TEM work, which is confirmed by the TG data, as shown in Fig. S6. Overall, the above results suggest a bi-phasic nickel and cobalt oxide structure for the comparison sample that primarily comprised oxide phases only.

To validate the structural merits of the hierarchically porous N-doped rGO nanofibers comprising hollow and ultrafine LDO nanocrystals as an advanced anode for LIBs, the electrochemical performance was analyzed using CR-2032 coin-type cells. The cyclic voltammetry (CV) curves for the cell utilizing P-(Ni, Co)O/rGO NFs were recorded for the initial 5 cycles at 0.1 mV s^{-1} in the voltage window of 0.001–3.0 V *vs.* Li^{+}/Li, and the results are presented in Fig. 5a. During the first CV scan, three reduction peaks were observed at 1.1, 0.85, and 0.45 V that correspond to three different redox processes: reduction of Co^{3+} to Co^{2+} at 1.1 V, conversion of $NiCo_2O_4$ into their respective metal species at 0.85 V, and further reduction of (Ni, Co)O phases to metallic species at 0.45 V [52,53]. However, during the anodic scan, the CV curve exhibits two broad peaks at 1.48 and 2.24 V, which correspond to the oxidation of metallic-Ni to NiO and metallic-Co to CoO, respectively [53,54]. From the second scan onward, only slight changes appeared in the CV profile, which was only observed in the cathodic region. For instance, the two cathodic peaks at 1.1 and 0.85 V during the first scan were merged into a single peak whereas the peak at 0.45 V disappeared completely, indicating a complete reduction of the oxide phases to their respective metallic species [55]. Afterward, almost overlapping and symmetrically shaped CV curves suggest highly reversible electrochemical processes inside the cell. In contrast, the CV profile for the F-(Ni, Co)O NF, that is, without LDH nanocrystals, is presented in Fig. S7. Compared to the P-(Ni, Co)O/rGO NF, the pristine sample displays two closely spaced cathodic peaks at 0.74 and 0.40 V, during the cathodic scan, which are attributed to the reduction of NiO and Co_3O_4 nanocrystals to their respective metallic species. Moreover, during the anodic scan, the two well-resolved peaks at 1.6 and 2.2 V are attributed to the oxidation of metallic species, similar to the P-(Ni, Co)O/rGO NF. Subsequently, the overlapping CV curves suggest similar electrochemical reaction processes. The CV results were further validated by analyzing the initial charge-discharge profiles at 1.0 A g^{-1} for P-(Ni, Co)O/rGO and pristine

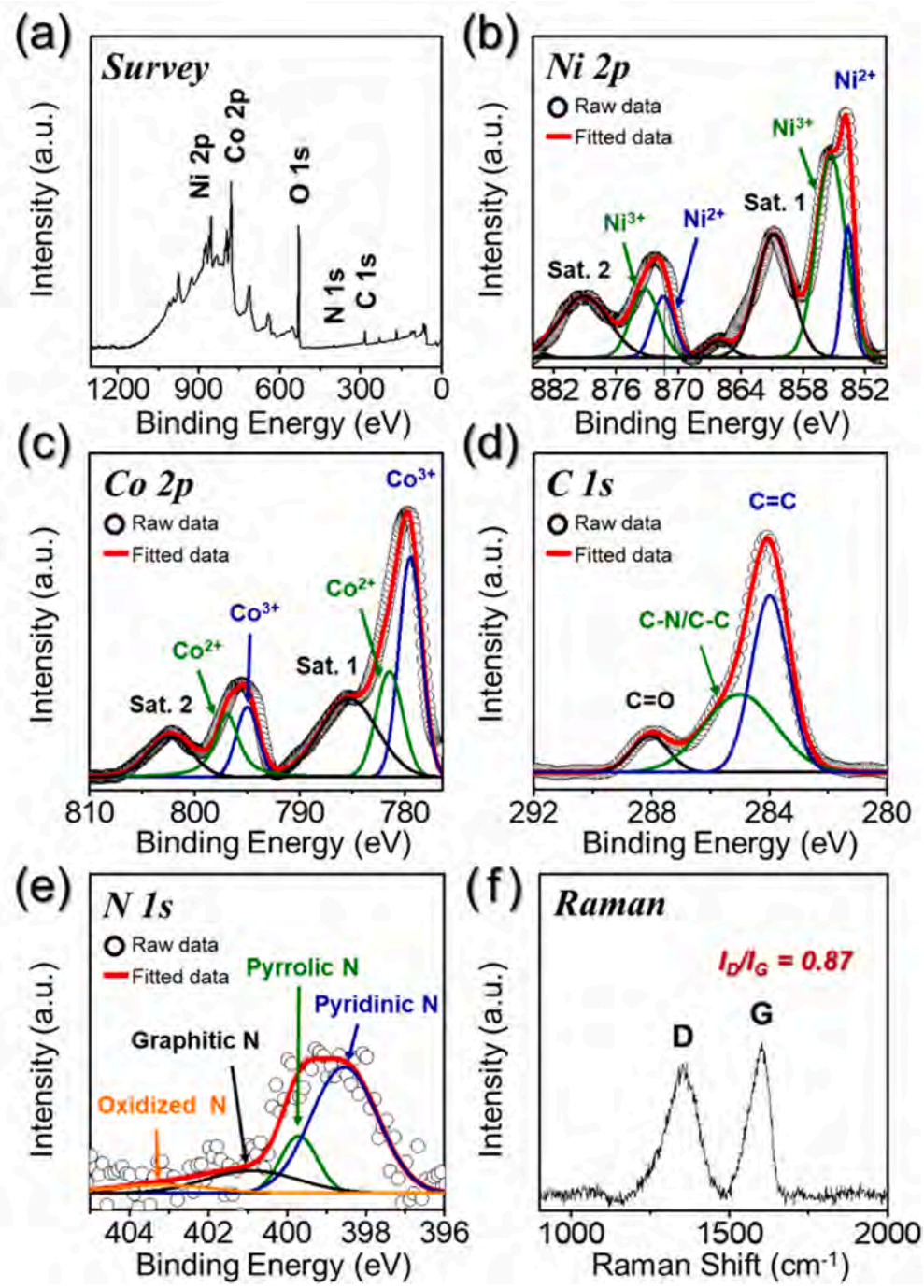

Fig. 4. (a) XPS survey spectrum, deconvoluted (b) Ni 2p, (c) Co 2p, (d) C 1s, (e) N 1s XPS spectra, and (f) Raman spectrum of the P-(Ni, Co)O/rGO NFs.

F-(Ni, Co)O NFs, as shown in Fig. 5b. The P-(Ni, Co)O/rGO NFs display two sloppy discharge plateaus at 1.1 and 0.85 V, which is consistent with the CV results. Furthermore, a third discharge plateau was observed at 0.57 V, suggesting the reduction of oxide species to their respective metallic nanograins and agrees with the CV results. In addition, a relatively longer discharge plateau length indicates that the majority of the redox processes took place at this potential. However, during the charge profile, no obvious plateaus were observed besides two short-length sloppy plateaus at 1.4 and 2.1 V, implying the oxidation of metallic species to their corresponding oxide phases. In contrast, the pristine F-(Ni, Co)O NFs exhibit two discharge plateaus at 0.89 and 0.56 V with shorter plateaus length, indicating their discharge capacity values will be lower than those of the P-(Ni, Co)O/rGO sample. Likewise, during the charge, the plateau at 2.13 V is in good accordance with the CV results. The charge/discharge capacities of the P-(Ni, Co)O/rGO and pristine F-(Ni, Co)O NFs were observed to be 1057/1534 and 597/959 mA h g^{-1}, respectively, with an initial Coulombic efficiency (CE) of 68.9 and 62.2%, respectively. In addition, the lower polarization potential of the P-(Ni, Co)O/rGO NFs ($\Delta V = 0.68$ V) compared to that of the pristine F-(Ni, Co)O NFs ($\Delta V = 1.71$ V) suggests it has comparatively better redox reaction kinetics. Overall, the CV and initial charge-discharge results suggest that the P-(Ni, Co)O/rGO NFs would exhibit enhanced electrochemical performance compared to the pristine F-(Ni, Co)O NFs.

To further explore the electrochemical stability of the P-(Ni, Co)O/rGO NFs, the long-term cycling performance was evaluated at 1.0 A g^{-1}, as shown in Fig. 5c. The cell with P-(Ni, Co)O/rGO NF anodes exhibited

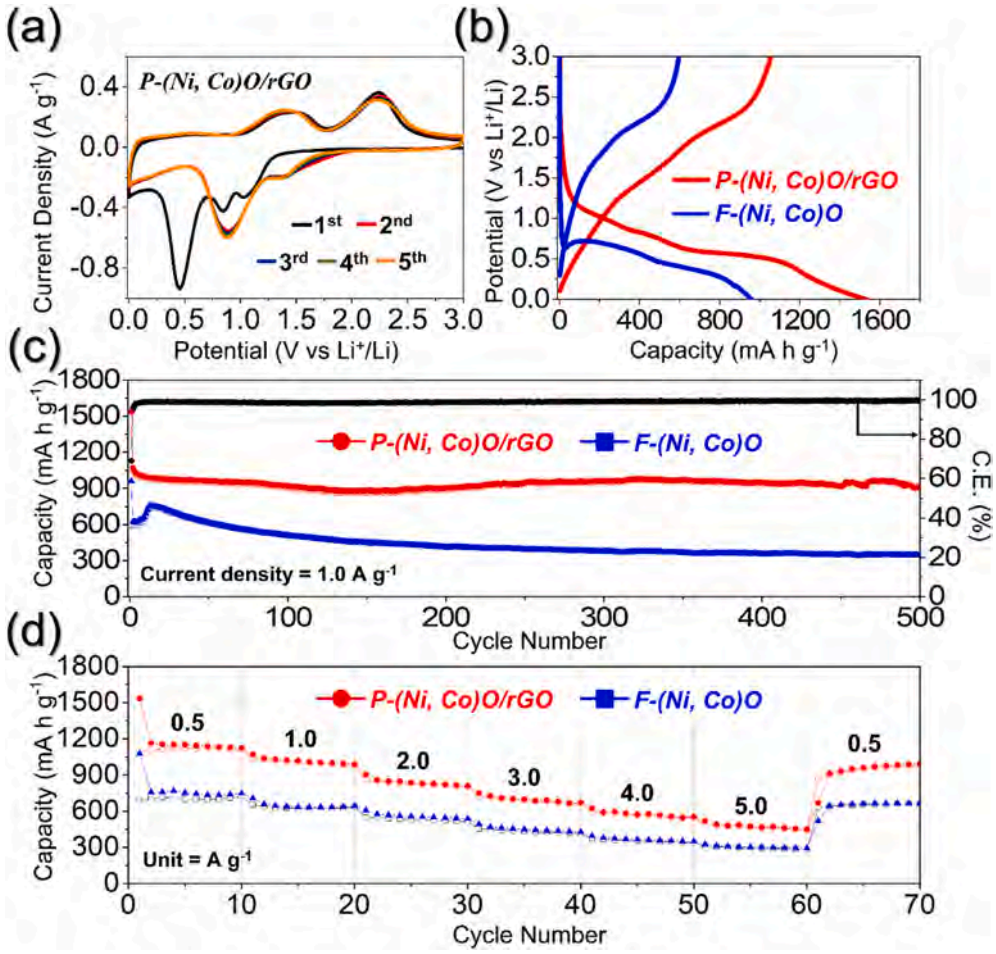

Fig. 5. Electrochemical performances of the P-(Ni, Co)O/rGO and F-(Ni, Co)O NFs as anodes: (a) cyclic voltammetry (CV) curves at 0.1 mV s^{-1} for initial five cycles for P-(Ni, Co)O/rGO NFs, (b) initial charge-discharge profiles at current density of 1.0 A g^{-1}, (c) long-term cycling performances at current density of 1.0 A g^{-1}, and (d) rate capability test at various current density rates.

a stable discharge capacity of 907 mA h g^{-1} at the end of the 500th cycle, which was exceptionally higher than that of the F-(Ni, Co)O NF anode, which displayed a discharge capacity of 345 mA h g^{-1} at an identical current density. Moreover, a low average discharge capacity decay rate of 0.08% signifies the structural merits of the P-(Ni, Co)O/rGO NF. In addition, a high Coulombic efficiency of 99.58% at the 500th cycle indicates highly reversible redox processes. The stable cycling performance of the P-(Ni, Co)O/rGO NFs could be attributed to the highly conductive self-supportive N-doped rGO matrix, which provides highly conductive channels for fast charge transfer. Additionally, the hierarchical porous structure offers sufficient space for efficient electrolyte percolation and channelizes the severe volume variation during repeated cycling. The rate performances of the two anode materials at various current densities in a stepwise manner are shown in Fig. 5d. The initial discharge capacity values for P-(Ni, Co)O/rGO NF were observed to be 1534, 1070, 904, 751, 625, and 519 mA h g^{-1} at current densities of 0.5, 1.0, 2.0, 3.0, 4.0, and 5.0 A g^{-1}, respectively. In contrast, the pristine F-(Ni, Co)O NF anode exhibits comparatively lower discharge capacities of 1077, 706, 607, 493, 396, and 327 mA h g^{-1} at current densities of 0.5, 1.0, 2.0, 3.0, 4.0, and 5.0 A g^{-1}, respectively. The exceptionally high discharge capacities of P-(Ni, Co)O/rGO NF, even at high current densities, clearly suggests that the structural benefits offer better electrolyte diffusion along with enhanced redox reaction kinetics, which validates the applicability of the sample as an advanced anode for LIBs. In addition, the electrochemical performance obtained in the present work is superior to that of previous studies, as shown in Table S2. It should also be noted that the obtained electrochemical performance is much better than the single metal oxide nanofibers (i.e., Co_3O_4) prepared using the identical synthesis process, as shown in Fig. S8.

The enhanced electrochemical performance of the P-(Ni, Co)O/rGO NF anode was further verified using the Li-ion kinetics studies shown in Fig. 6. The CV curves were obtained for the Li-ion cell employing P-(Ni, Co)O/rGO NF as an advanced anode at different voltage scan rates in the voltage window of 0.001–3.0 V (Fig. 6a). Furthermore, the graphs between the redox peak current (i) and scan rates (v) were plotted using the obtained CV curves to distinguish the surface-controlled processes from the diffusion-controlled process. The i versus v relationship was examined using the following equation: $i = av^b$ and $\log(i) = b\log(v) + \log(a)$, where a and b are variables that were determined from the graphs [56]. The b values indicate whether the reaction processes are surface-controlled or diffusion-controlled. It has been reported that a b value close to 0.5 implies reaction kinetics dominated by diffusion processes, whereas a b value of 1.0 implies surface-controlled or capacitive processes [30]. The CV curves shown in Fig. 6a indicate that the anodic and cathodic peak pairs are symmetrically positioned, even at a high voltage scan rate of 2.0 mV s^{-1}. In addition, the b values for the redox peaks 1, 2, 3, and 4 (Fig. 6b) were determined using the log (i) *vs.* log (v) slope and found to be 0.82, 0.70, 0.84, and 0.85, respectively, which are close to 1.0, implying that the redox processes are mainly dominated by surface-controlled effects. In contrast, the CV curves for F-(Ni, Co)O NF display slightly unresolved anodic/cathodic peaks with b values close to 0.5 (Figs. S9a and S9b), suggesting diffusion-induced kinetics. Furthermore, it has been reported that capacitive-induced

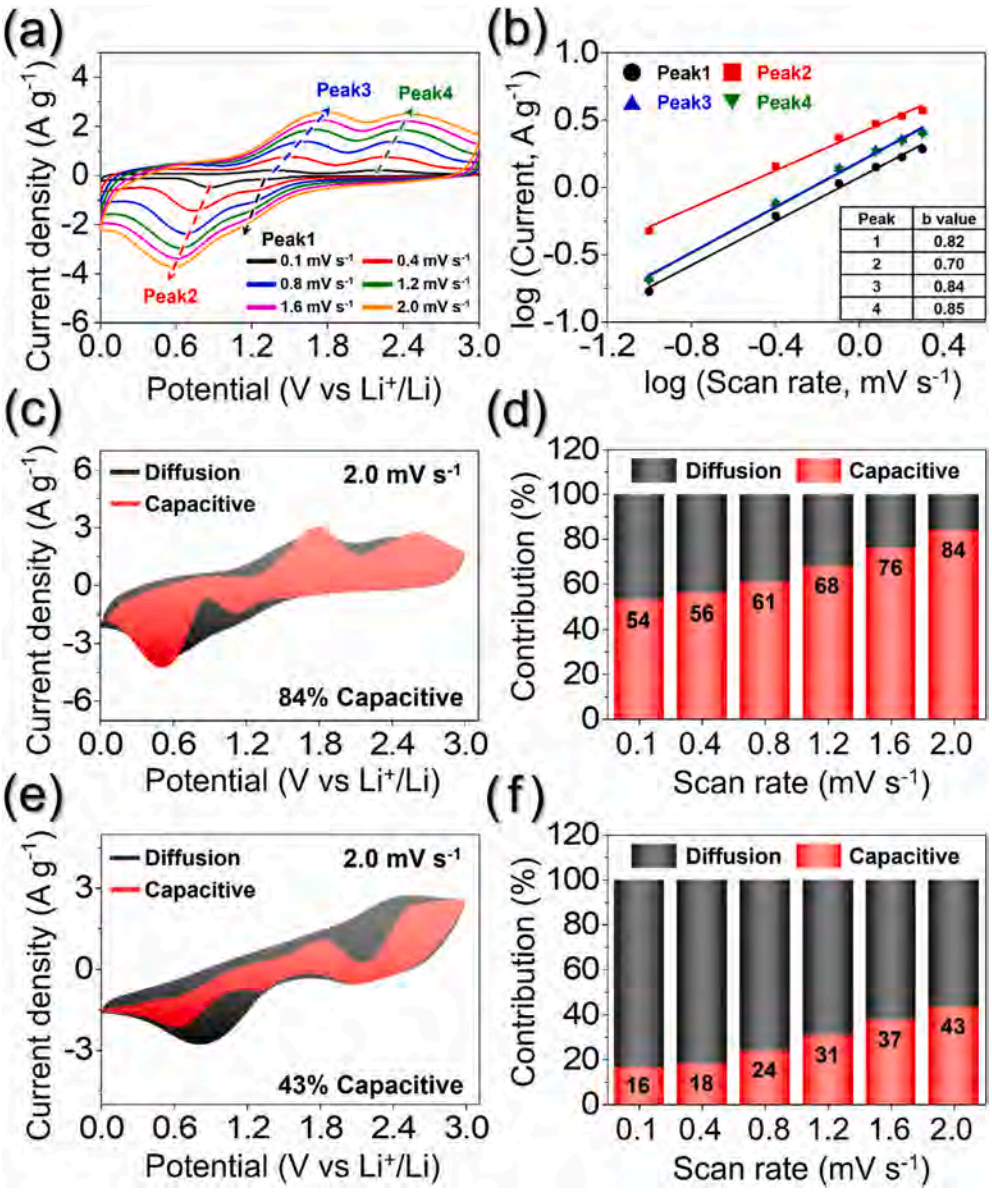

Fig. 6. Redox reaction kinetics of the (a–d) P-(Ni, Co)O/rGO NF and (e, f) F-(Ni, Co)O NF: (a) CV curves at different scan rates, (b) plot between log (*i*) *vs.* log (scan rate) for each redox peak, (c) capacitive contribution highlighted in red color area at 2.0 mV s^{-1}, (d) bar graph showing the capacitive fraction at various scan rates, and (e, f) capacitive contribution and bar graph representation at 2.0 mV s^{-1} and different scan rates, respectively for F-(Ni, Co)O NF. (For interpretation of the references to color in this figure legend, the reader is referred to the Web version of this article.)

reaction kinetics are more favorable than diffusion-controlled kinetics for the overall enhanced electrochemical performance of the cells. Therefore, it is imperative to separate the capacitive-controlled processes from the diffusion-controlled processes in the total storage charge to analyze the transport kinetics in a more detailed manner. The quantitative analysis of the surface-controlled processes was performed using the following relation: $i = k_1\nu + k_2\nu^{1/2}$, where $k_1\nu$ and $k_2\nu^{1/2}$ represent the contributions from the capacitive and diffusion-controlled processes, respectively [30]. As shown in Fig. 6c, the capacitive contribution of P-(Ni, Co)O/rGO NF was *ca.* 84%, which is consistent with the high *b* values in Fig. 6b. On the other hand, the percentage of the capacitive process in pristine F-(Ni, Co)O NF was very low (only 43%, which is almost half of the main sample), as shown in Fig. 6e. Likewise, the capacitive contributions of the P-(Ni, Co)O/rGO NF at different scan rates were determined and are summarized in Fig. 6d. High capacitive contribution values of 54%, 56%, 61%, 68%, 76%, and 84% at scan rates of 0.1, 0.4, 0.8, 1.2, 1.6, and 2.0 mV s^{-1}, respectively, were obtained for the P-(Ni, Co)O/rGO NF while low capacitive contribution values of 16%, 18%, 24%, 31%, 37%, and 43% were obtained for pristine F-(Ni, Co)O NF (Fig. 6f) at identical voltage scan rates. The relatively higher percentage of the capacitive-controlled contribution of P-(Ni, Co)O/rGO NF clearly indicates that its structural supremacy will eventually result in kinetically favored fast ionic transport, thereby enhancing the rate capability and long-term cycling performance. The synergistic effects of the hierarchical porous and highly conductive nanostructure simultaneously provide numerous channels for efficient electrolyte percolation and faster Li-ion diffusion during the redox processes owing to the short diffusion pathways.

The superior Li-ion kinetics for P-(Ni, Co)O/rGO NF were further supported by the Nyquist plots obtained using the EIS measurements of a fresh cell and one subjected to different cycling numbers at a current density of 1.0 A g^{-1}. The equivalent circuit model used for the Nyquist plot fitting is shown in Fig. S10. The various fitted parameters for the Nyquist plots of the two samples are listed in Table S3. The Nyquist plots of the fresh cell in Fig. 7a exhibit a similar low-frequency intercept on the *x*-axis, which is the solution resistance (R_s) of the cell and suggests similar electrode-electrolyte interface characteristics [57]. In addition, a depressed semicircle in the mid-frequency region can be used to measure the charge-transfer resistance (R_{ct}) of the cell, which was 230 Ω for the P-(Ni, Co)O/rGO NF and 180 Ω for the pristine F-(Ni, Co)O NF. The higher R_{ct} of the P-(Ni, Co)O/rGO NF is attributed to its higher surface area compared to the F-(Ni, Co)O NF, which subsequently resulted in

slightly larger polarization in the OCV state [58,59]. However, the R_{ct} values after the 5th cycle (Fig. 7b) decreased sharply for both the samples, with P-(Ni, Co)O/rGO NFs displaying a lower value (25 Ω) than the F-(Ni, Co)O sample (40 Ω), which was due to the formation of a stable solid electrolyte interphase (SEI) layer in the P-(Ni, Co)O/rGO NFs [60]. Furthermore, after the 100th cycle (Fig. 7c), the R_{ct} of the F-(Ni, Co)O NF was significantly higher than that of the P-(Ni, Co)O/rGO NFs, which clearly demonstrates the structural superiority of the P-(Ni, Co)O/rGO NFs over prolonged cycling. These results indicate that the high electrical conductivity of P-(Ni, Co)O/rGO supports faster charge transfer properties in addition to increasing the structural integrity of the nanofibers. This could be attributed to the highly conductive N-doped rGO matrix, which also acts as a self-supportive scaffold to prevent the nanostructure from collapsing during repeated cycling. The plot describing the relationship between Z_{re} and $\omega^{-1/2}$ in the low-frequency region is shown in Fig. 7d. The plots indicate that the P-(Ni, Co)O/rGO NFs exhibit a less steep slope compared to the F-(Ni, Co)O NF, implying that they experience a higher Li-ion diffusion owing to their porous and highly conductive nanostructures. To validate these results, Li-ion diffusion coefficient (D_{Li}^{+}) values were calculated using the following relation: $D = 0.5R^2T^2/A^2F^4C^2\sigma_W^2$, where D is the Li-ion diffusion (D_{Li}^{+}) coefficient, R is the gas constant (8.314 J mol^{-1} K^{-1}), T is the absolute

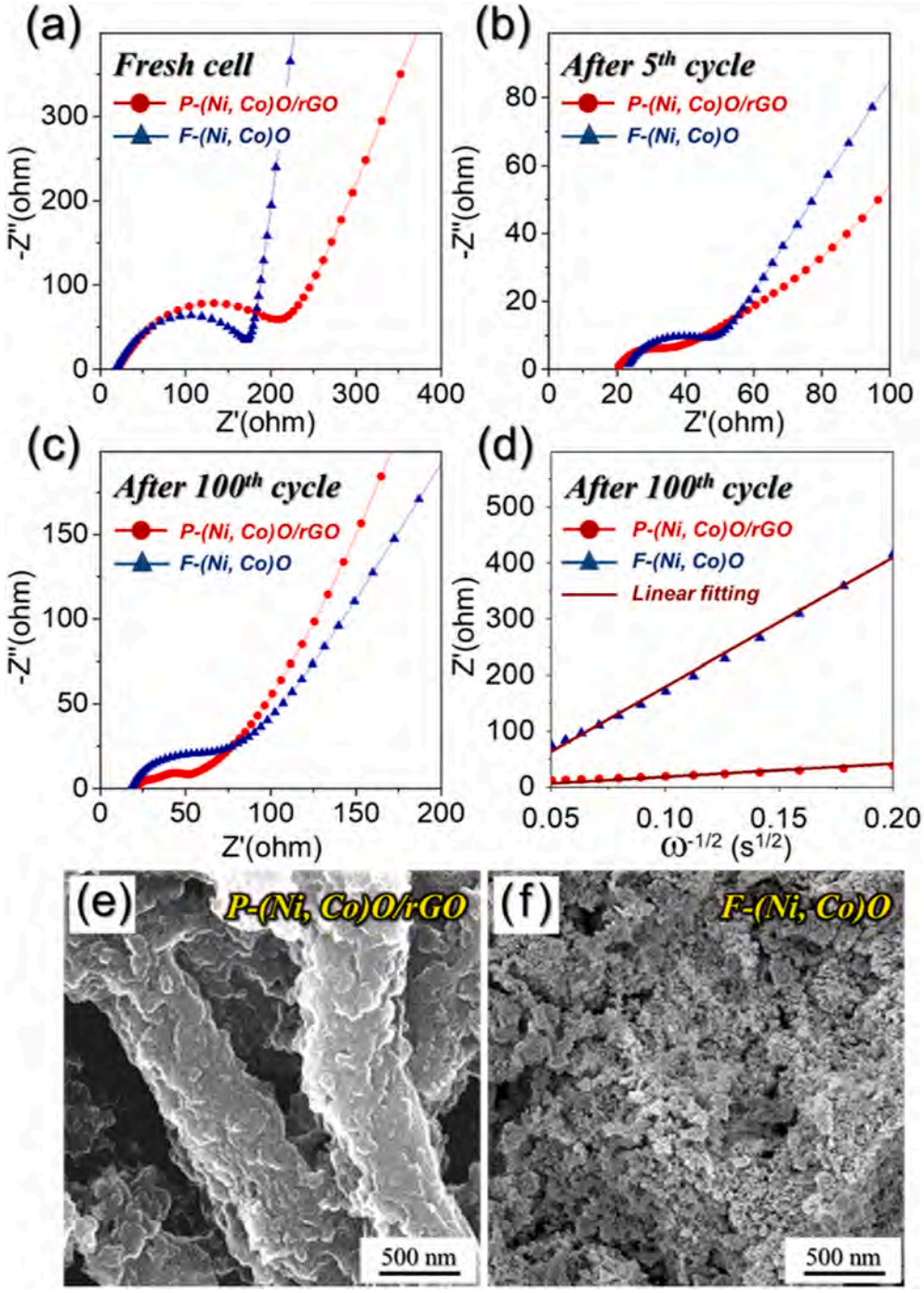

Fig. 7. Nyquist impedance plot comparison for different anodes: (a) For fresh cell, (b) after 5th cycle, (c) after 100th cycle, (d) relationship plot between real part of the impedance (Z') and $w^{-1/2}$ at the end of 100th cycle, and (e, f) FE-SEM morphologies of the cycled electrodes after 100th cycle for (e) P-(Ni, Co)O/rGO and (f) F-(Ni, Co)O NFs.

temperature (298 K), A is the area of the electrode (1.5386 cm^2), C is the Li-ion concentration (1.0 mol L^{-1}), F is the Faraday constant (96,485 C mol^{-1}), and σ_W is the Warburg impedance factor, which can be calculated from the slope of the following equation: $Z' = R_s + R_{ct} + \sigma_W \omega^{-0.5}$ [61]. The diffusion coefficient values obtained using the above equations were 2.5 x 10^{-13} and 2.6 x 10^{-15} cm^2 s^{-1} for P-(Ni, Co)O/rGO NF and F-(Ni, Co)O NF, respectively. Therefore, the two-order higher $D_{Li}{}^+$ value for P-(Ni, Co)O/rGO NF compared to F-(Ni, Co)O NF clearly suggests enhanced Li-ion diffusion occurs in the P-(Ni, Co)O/rGO NF, which eventually results in improved redox reaction kinetics. This is attributed to the highly conductive N-doped rGO matrix that provides conductive pathways during the redox processes and, hence, higher Li-ion diffusivity. Moreover, the $D_{Li}{}^+$ values in the present work are either comparable or better than those reported in previous studies on various anode materials [62,63]. To investigate the structural stability of the NFs, the post-cycling morphologies of the P-(Ni, Co)O/rGO NF and F-(Ni, Co)O NF were examined after 100 cycles, as shown in Fig. 7e and f. The P-(Ni, Co)O/rGO NF maintained its fibrous morphology (Fig. 7e) even after continuous cycling. This proves that the integrity of the robust structure remains intact, which is due to the rGO matrix that acts as a self-supporting skeleton and prevents the nanostructure from collapsing during repeated cycling. In contrast, the pristine F-(Ni, Co)O NF displays aggregated particle-type morphologies, implying that the nanostructure breaks down owing to the severe volume stress it experiences during cycling. Therefore, the above results imply that the structural supremacy of the P-(Ni, Co)O/rGO NF resulted in an improved electrochemical performance, with high rate capability and considerable cycling stability.

Overall, the unique structural design strategy adopted to obtain hierarchically porous N-doped rGO nanofibers comprising MOF-derived hollow and ultrafine LDO nanocrystals resulted in an enhanced overall performance. The robust structure based on the self-supporting N-doped rGO nanofiber framework not only provides structural integrity to the nanostructure to prevent it from collapsing during the redox process but also offers enormous conducting channels for fast charge transfer kinetics. In addition, the porous structure guarantees short diffusion pathways, which eventually allows efficient Li-ion diffusion owing to the better penetration of the electrolyte and, therefore, superior reaction kinetics.

4. Conclusions

In summary, we developed multicomponent and hierarchical porous N-doped rGO nanofibers comprising MOF-derived hollow and ultrafine LDO nanocrystals [denoted as P-(Ni, Co)O/rGO NF] as an advanced anode for LIBs. The rational nanostructure contains highly conductive and hierarchically porous N-doped rGO as a self-supporting scaffold that provides mechanical integrity to the nanofibers and offers numerous conducting pathways together with efficient electrolyte penetration. Furthermore, the hollow and ultrafine layered double metal (Ni, Co) oxide nanocrystals derived from the MOF-based hollow-LDH nanostructure as a precursor provide sufficient space for substantial ion-exchange sites and the alleviation of severe volume stress. Benefitting from the unique nanostructure synthetic strategy, the robust nanofiber displays an exceptional electrochemical performance, a stable cycling performance, and considerable rate capabilities, which are primarily attributed to the high Li-ion diffusion coefficients. The design of the novel structure presented in this work will instruct the design of porous and highly conducting advanced materials for various energy storage systems.

CRediT authorship contribution statement

Chan Sic Kim: Conceptualization, Methodology, Data curation, Writing – original draft, Visualization, Investigation. **Jae Seob Lee:** Conceptualization, Methodology, Data curation, Writing – original draft, Visualization, Investigation. **Rakesh Saroha:** Conceptualization, Data curation, Writing – original draft, Writing – review & editing. **Yoon Beom Park:** Methodology, Data curation, Investigation. **Yun Chan Kang:** Conceptualization, Supervision. **Dong-Won Kang:** Data curation, Investigation. **Sang Mun Jeong:** Supervision, Funding acquisition. **Jung Sang Cho:** Conceptualization, Methodology, Investigation, Writing – review & editing, Supervision, Funding acquisition.

Declaration of competing interest

The authors declare that they have no known competing financial interests or personal relationships that could have appeared to influence the work reported in this paper.

Acknowledgments

C.S. Kim and J.S. Lee contributed equally to this work. This work was supported by a National Research Foundation of Korea (NRF) grant funded by the Korean government (MSIP) (NRF-2021R1A4A2001687, NRF-2021R1I1A3057700).

Appendix A. Supplementary data

Supplementary data to this article can be found online at https://doi.org/10.1016/j.jpowsour.2022.231030.

References

[1] R. Saroha, A.K. Panwar, Y. Sharma, P.K. Tyagi, S. Ghosh, Development of surface functionalized ZnO-doped $LiFePO_4$/C composites as alternative cathode material for lithium ion batteries, Appl. Surf. Sci. 394 (2017) 25–36.
[2] Q.N. Tran, I.T. Kim, J. Hur, J.H. Kim, H.W. Choi, S.J. Park, Composite of nanocrystalline cellulose with tin dioxide as lightweight substrates for high-performance lithium-ion battery, Kor. J. Chem. Eng. 37 (5) (2020) 898–904.
[3] H. Niaz, M.M. Lakouraj, J. Liu, Techno-economic feasibility evaluation of a standalone solar-powered alkaline water electrolyzer considering the influence of battery energy storage system: a Korean case study, Kor. J. Chem. Eng. 38 (2021) 1617–1630.
[4] S.H. Kim, Y.R. Choi, Y.J. Cho, S.Y. Rhyu, S.W. Kang, Effective pore control and enhanced strength of cellulose acetate using polyethylene glycol for improved battery stability, Kor. J. Chem. Eng. 38 (8) (2021) 1715–1719.
[5] Q. Wang, D. O'Hare, Recent advances in the synthesis and application of layered double hydroxide (LDH) nanosheets, Chem. Rev. 112 (2012) 4124–4155.
[6] N.A. Jose, H.C. Zeng, A.A. Lapkin, Hydrodynamic assembly of two-dimensional layered double hydroxide nanostructures, Nat. Commun. 9 (2018) 4913–4924.
[7] X. Xuan, M. Qian, L. Han, L. Wan, Y. Li, T. Lu, L. Pan, Y. Niu, S. Gong, In-situ growth of hollow NiCo layered double hydroxide on carbon substrate for flexible supercapacitor, Electrochim. Acta 321 (2019) 134710–134726.
[8] K.K. Sarigamala, S. Shukla, A. Struck, S. Saxena, Rationally engineered 3D-dendritic cell-like morphologies of LDH nanostructures using graphene-based core–shell structure, Microsyst. Nanoeng. 5 (2019) 65–73.
[9] Y. Zhou, J. Li, Y. Yang, B. Luo, X. Zhang, E. Fong, W. Chu, K. Huang, Unique 3D flower-on-sheet nanostructure of NiCo LDHs: controllable microwave-assisted synthesis and its application for advanced supercapacitors, J. Alloys Compd. 788 (2019) 1029–1036.
[10] C. Duan, L. Wang, J. Liu, Y. Qu, J. Gao, Y. Yang, B. Wang, J. Li, L. Zheng, M. Li, 3D Carbon electrode with hierarchical nanostructure based on NiCoP core-layered double hydroxide shell for supercapacitors and hydrogen evolution, Chemelectrochem 8 (2021) 2272–2281.
[11] J.-G. Seong, T.H. Ko, D. Lei, W.-K. Choi, Y.-S. Kuk, M.-K. Seo, B.-S. Kim, Engineered NiCo-LDH nanosheets- and $ZnFe_2O_4$ nanocubes-decorated carbon nanofiber bonded mats for high-rate asymmetric supercapacitors, Green Energy Environ (2021). In press.
[12] M. Ding, P. Wang, Z. Zhang, L. Yin, Metal–organic framework-derived porous NiCo-layered double hydroxide@MnO_2 hierarchical nanostructures as catalytic cathodes for long-life Li–O_2 batteries, ACS Appl. Energy Mater. 4 (2021) 61–71.
[13] R. Saroha, J.H. Oh, Y.H. Seon, Y.C. Kang, J.S. Lee, J.S. Cho, Freestanding interlayers for Li–S batteries: design and synthesis of hierarchically porous N-doped C nanofibers comprising vanadium nitride quantum dots and MOF-derived hollow N-doped C nanocages, J. Mater. Chem. A 9 (2021) 11651–11664.
[14] L. Zhang, H. Zhou, R. Li, H. Cheng, S. Wang, B. Chen, Y. Zhuang, J. Chen, A. Yuan, Co/CoOx Heterojunctions encapsulated N-doped carbon sheets via a dual-template-guided strategy as efficient electrocatalysts for rechargeable Zn-air battery, J. Colloid Interface Sci. 599 (2021) 46–57.
[15] L. Zhong, H. Zhou, R. Li, T. Bian, S. Wang, A. Yuan, In situ confinement pyrolysis of ZIF-67 nanocrystals on hollow carbon spheres towards efficient electrocatalysts for oxygen reduction, J. Colloid Interface Sci. 584 (2021) 439–448.

[16] J. Feng, H. Zhou, D. Chen, T. Bian, A. Yuan, Core-shell structured ZnCo/NC@MoS_2 electrocatalysts for tunable hydrogen evolution reaction, Electrochim. Acta 331 (2020) 135445–135453.

[17] J. Shao, J. Feng, H. Zhou, A. Yuan, Graphene aerogel encapsulated Fe-Co oxide nanocubes derived from prussian blue analogue as integrated anode with enhanced Li-ion storage properties, Appl. Surf. Sci. 471 (2019) 745–752.

[18] X. Wang, F. Huang, F. Rong, P. He, R. Que, Unique MOF-derived hierarchical MnO_2 nanotubes@NiCo-LDH/CoS_2 nanocage materials as high performance supercapacitors, J. Mater. Chem. A 7 (2019) 12018–12028.

[19] S. Zhang, Y. Zhao, Q. Yin, J. Zhang, K. Wang, J. Hang, Hollow ZIF-67-C/LDO core/shell heterostructure as a high-performance anode material for sodium ion batteries, Mater. Lett. 294 (2021) 129817–129820.

[20] R. Zhang, Z. Xue, J. Qin, M. Sawangphruk, X. Zhang, R. Liu, NiCo-LDH/Ti_3C_2 MXene hybrid materials for lithium ion battery with high-rate capability and long cycle life, J. Energy Chem. 50 (2020) 143–153.

[21] S.H. Oh, M.S. Jo, S.M. Jeong, Y.C. Kang, J.S. Cho, Hierarchical yolk-shell CNT-(NiCo)O/C microspheres prepared by one-pot spray pyrolysis as anodes in lithium-ion batteries, Chem. Eng. J. 368 (2019) 438–447.

[22] X. Zhang, B. Dai, S. Ren, Z. Hu, X. Zheng, Y. Wang, H. Sun, D. Niu, L. Wang, Iron diffusion-doped magnesium-aluminum layered double oxides as a multifunctional adsorbent for removal of F^-, Sb(III) and methyl orange contaminants from water, Kor. J. Chem. Eng. 37 (2020) 792–803.

[23] H. Song, J. Su, C. Wang, In situ subangstrom-thick organic engineering enables mono-scale, ultrasmall ZnO nanocrystals for a high initial coulombic efficiency, fully reversible conversion, and cycle-stable Li-ion storage, Adv. Energy Mater. 9 (19) (2019) 1900426–1900433.

[24] J. Su, H. Song, C. Wang, Morphology reshaping enabling self-densification of manganese oxide hybrid materials for high-density lithium storage anodes, Adv. Funct. Mater. 29 (51) (2019) 1907154–1907163.

[25] H. Song, J. Su, C. Wang, Hybrid solid electrolyte interphases enabled ultralong life Ca-metal batteries working at room temperature, Adv. Mater. 33 (2) (2021) 2006141–2006148.

[26] H. Song, J. Su, C. Wang, Multi-ions electrolyte enabled high performance voltage tailorable room-temperature Ca-metal batteries, Adv. Energy Mater. 11 (10) (2021) 2170037–2170045.

[27] M.S. Jo, S. Ghosh, S.M. Jeong, Y.C. Kang, J.S. Cho, Coral-like yolk–shell-structured nickel oxide/carbon composite microspheres for high-performance Li-ion storage anodes, Nano-Micro Lett. 11 (3) (2019) 1–18.

[28] G.D. Park, J.S. Cho, Y.C. Kang, Multiphase and double-layer $NiFe_2O_4$@NiO-hollow-nanosphere-decorated reduced graphene oxide composite powders prepared by spray pyrolysis applying nanoscale kirkendall diffusion, ACS Appl. Mater. Interfaces 7 (30) (2015) 16842–16849.

[29] H. Hu, J. Liu, Z. Xu, L. Zhang, B. Cheng, W. Ho, Hierarchical porous Ni/Co-LDH hollow dodecahedron with excellent adsorption property for Congo red and Cr(VI) ions, Appl. Surf. Sci. 478 (2019) 981–990.

[30] J.S. Lee, M.S. Jo, R. Saroha, D.S. Jung, Y.H. Seon, J.S. Lee, Y.C. Kang, D.W. Kang, J. S. Cho, Hierarchically well-developed porous graphene nanofibers comprising N-doped graphitic C-coated cobalt oxide hollow nanospheres as anodes for high-rate Li-ion batteries, Small 16 (32) (2020) 2002213–2002226.

[31] S. Sundriyal, V. Shrivastav, H. Kaur, S. Mishra, A. Deep, High-performance symmetrical supercapacitor with a combination of a ZIF-67/rGO composite electrode and a redox additive electrolyte, ACS Omega 3 (12) (2018) 17348–17358.

[32] C. Lu, Y. Yan, T. Zhai, Y. Fan, W. Zhou, 2-nm-thick NiCo LDH@NiSe single-crystal nanorods grown on Ni foam as integrated electrode with enhanced areal capacity for supercapacitors, Batter. Supercaps 3 (2020) 534–540.

[33] R. Valdez, D.B. Grotjahn, D.K. Smith, J.M. Quintana, A. Olivas, Nanosheets of Co-(Ni and Fe) layered double hydroxides for electrocatalytic water oxidation reaction, Int. J. Electrochem. Sci. 10 (2015) 909–918.

[34] A. Tang, P. Chen, C. Mi, Ni-Co layered double hydroxide nanosheet array on nickel foam coated graphene for high-performance asymmetric supercapacitors, Ionics 26 (2020) 6277–6287.

[35] X. Wang, X. Li, X. Du, X. Ma, X. Hao, C. Xue, H. Zhu, S. Li, Controllable synthesis of NiCo LDH nanosheets for fabrication of high-performance supercapacitor electrodes, Electroanalysis 29 (2017) 1286–1293.

[36] B. Ali, S.M. Tasirin, P. Aminayi, Z. Yaakob, N.T. Ali, W. Noori, Non-supported nickel-based coral sponge-like porous magnetic alloys for catalytic production of syngas and carbon bio-nanofilaments via a biogas decomposition approach, Nanomaterials 8 (12) (2018) 1053–1080.

[37] X. Hu, P. Li, X. Zhang, B. Yu, C. Lv, N. Zeng, J. Luo, Z. Zhang, J. Song, Y. Liu, Ni-Based catalyst derived from NiAl layered double hydroxide for vapor phase catalytic exchange between hydrogen and water, Nanomaterials 9 (12) (2019) 1688–1702.

[38] Q. Li, J.-B. Song, S.-C. Li, Y.-S. Yang, Q. Gao, F. Yu Wang, La-enhanced Ni nanoparticles highly dispersed on SiC for low-temperature CO methanation performance, Rare Met. 40 (2021) 1753–1761.

[39] Á.A. Amaya, C.A. González, M.E. Niño-Gómez, F. Martínez O, XPS fitting model proposed to the study of Ni and La in deactivated FCC catalysts, J. Electron. Spectrosc. Relat. Phenom. 233 (2019) 5–10.

[40] J. Zhang, Q. Mei, Y. Ding, K. Guo, X. Yang, J. Zhao, Ordered mesoporous $NiCo_2O_4$ nanospheres as a novel electrocatalyst platform for 1-naphthol and 2-naphthol individual sensing application, ACS Appl. Mater. Interfaces 9 (2017) 29771–29781.

[41] Y. Wang, L. Wang, B. Wei, Q. Miao, Y. Yuan, Z. Yang, W. Fei, Electrodeposited nickel cobalt sulfide nanosheet arrays on 3D-graphene/Ni foam for high-performance supercapacitors, RSC Adv. 5 (2015) 100106–100113.

[42] A.A. Khaleed, A. Bello, J.K. Dangbegnon, M. Madito, O. Olaniyan, F. Barzegar, K. Makgopa, K.O. Oyedotun, B.W. Mwakikunga, S. Ray, Solvothermal synthesis of surfactant free spherical nickel hydroxide/graphene oxide composite for supercapacitor application, J. Alloys Compd. 721 (2017) 80–91.

[43] R. Gao, L. Pan, H. Wang, Y. Yao, X. Zhang, L. Wang, J.J. Zou, Breaking trade-off between selectivity and activity of nickel-based hydrogenation catalysts by tuning both steric effect and d-band center, Adv. Sci. 6 (10) (2019) 1900054–1900063.

[44] X. Xu, L. Li, F. Yu, H. Peng, X. Fang, X. Wang, Mesoporous high surface area NiO synthesized with soft templates: remarkable for catalytic CH_4 deep oxidation, Mol. Catal. 441 (2017) 81–91.

[45] H. Wang, X. Fan, X. Zhang, Y. Huang, Q. Wu, Q. Pan, Q. Li, In situ growth of NiO nanoparticles on carbon paper as a cathode for rechargeable Li–O_2 batteries, RSC Adv. 7 (2017) 23328–23333.

[46] R. Saroha, J.H. Oh, J.S. Lee, Y.C. Kang, S.M. Jeong, D.-W. Kang, C. Cho, J.S. Cho, Hierarchically porous nanofibers comprising multiple core–shell Co_3O_4@graphitic carbon nanoparticles grafted within N-doped CNTs as functional interlayers for excellent Li–S batteries, Chem. Eng. J. 426 (2021) 130805–130818.

[47] S. Li, S. Peng, L. Huang, X. Cui, A.M. Al-Enizi, G. Zheng, Carbon-coated Co^{3+}-rich cobalt selenide derived from ZIF-67 for efficient electrochemical water oxidation, ACS Appl. Mater. Interfaces 8 (2016) 20534–20539.

[48] M. Cheng, H. Fan, Y. Song, Y. Cui, R. Wang, Interconnected hierarchical $NiCo_2O_4$ microspheres as high-performance electrode materials for supercapacitors, Dalton Trans. 46 (2017) 9201–9209.

[49] Y. Zhang, L. Sun, L. Zhang, X. Li, J. Gu, H. Si, L. Wu, Y. Shi, C. Sun, Y. Zhang, Highly porous oxygen-doped NiCoP immobilized in reduced graphene oxide for supercapacitive energy storage, Compos. B Eng. 182 (2020) 107611–107653.

[50] M.S. Jo, J.S. Lee, S.Y. Jeong, J.K. Kim, Y.C. Kang, D.W. Kang, S.M. Jeong, J.S. Cho, Golden bristlegrass-like hierarchical graphene nanofibers entangled with N-doped CNTs containing $CoSe_2$ nanocrystals at each node as anodes for high-rate sodium-ion batteries, Small 16 (38) (2020) 2003391–2003406.

[51] R. Saroha, A.K. Panwar, Effect of in situ pyrolysis of acetylene (C_2H_2) gas as a carbon source on the electrochemical performance of $LiFePO_4$ for rechargeable lithium-ion batteries, J. Phys. D Appl. Phys. 50 (2017) 255501–255513.

[52] S.-K. Park, J.K. Kim, Y.C. Kang, Metal–organic framework-derived $CoSe_2$/(NiCo)Se_2 box-in-box hollow nanocubes with enhanced electrochemical properties for sodium-ion storage and hydrogen evolution, J. Mater. Chem. A 5 (2017) 18823–18830.

[53] J. Leng, Z. Wang, X. Li, H. Guo, H. Li, K. Shih, G. Yan, J. Wang, Accurate construction of a hierarchical nickel–cobalt oxide multishell yolk–shell structure with large and ultrafast lithium storage capability, J. Mater. Chem. A 5 (2017) 14996–15001.

[54] K. Cao, L. Jiao, Y. Liu, H. Liu, Y. Wang, H. Yuan, Ultra-high capacity lithium-ion batteries with hierarchical CoO nanowire clusters as binder free electrodes, Adv. Funct. Mater. 25 (7) (2015) 1082–1089.

[55] X. Yin, C. Zhi, W. Sun, L.-P. Lv, Y. Wang, Multilayer NiO@Co_3O_4@graphene quantum dots hollow spheres for high-performance lithium-ion batteries and supercapacitors, J. Mater. Chem. A 7 (2019) 7800–7814.

[56] J.S. Lee, R. Saroha, S.H. Oh, D.H. Shin, S.M. Jeong, J.K. Kim, J.S. Cho, Rational design of perforated bimetallic (Ni, Mo) sulfides/N-doped graphitic carbon composite microspheres as anode materials for superior Na-ion batteries, Small Methods 5 (9) (2021) 2100195–2100209.

[57] R. Saroha, A. Gupta, A.K. Panwar, Electrochemical performances of Li-rich layered-layered Li_2MnO_3-$LiMnO_2$ solid solutions as cathode material for lithium-ion batteries, J. Alloys Compd. 696 (2017) 580–589.

[58] C. Wang, D. Wang, Q. Wang, H. Chen, Fabrication and lithium storage performance of three-dimensional porous NiO as anode for lithium-ion battery, J. Power Sources 195 (21) (2010) 7432–7437.

[59] J.S. Cho, J.-K. Lee, Y.C. Kang, Graphitic carbon-coated $FeSe_2$ hollow nanosphere-decorated reduced graphene oxide hybrid nanofibers as an efficient anode material for sodium ion batteries, Sci. Rep. 6 (1) (2016) 1–13.

[60] T.S. Pathan, M. Rashid, M. Walker, W.D. Widanage, E. Kendrick, Active formation of Li-ion batteries and its effect on cycle life, J. Phys. Energy 1 (4) (2019), 044003-044023.

[61] R. Saroha, A.K. Panwar, Y. Sharma, Physicochemical and electrochemical performance of $LiFe_{1-x}Ni_xPO_4$ ($0 \leq x \leq 1.0$) solid solution as potential cathode material for rechargeable lithium-ion battery, Ceram. Int. 43 (7) (2017) 5734–5742.

[62] Y.-S. Lee, K.-S. Ryu, Study of the lithium diffusion properties and high rate performance of $TiNb_6O_{17}$ as an anode in lithium secondary battery, Sci. Rep. 7 (16617) (2017) 1–13.

[63] F.N. Sayed, M. Sreedhara, A. Soni, U. Bhat, R. Datta, A.J. Bhattacharyya, C. Rao, Li and Na-ion diffusion and intercalation characteristics in vertically aligned TiS_2 nanowall network grown using atomic layer deposition, Mater. Res. Express 6 (11) (2019) 115549–115560.